Research Square

Preprints are preliminary reports that have not undergone peer review.
They should not be considered conclusive, used to inform clinical practice,
or referenced by the media as validated information.

The roles of nonharmonic damping and spatial correlation of atomic movements in determining the amplitudes and attenuation frequencies of electro-optic coefficients

Mouyi Weng

mouyiweng@semi.ac.cn

Institute of Semiconductors, Chinese Academy of Sciences

Linwang Wang

Institute of Semiconductors, Chinese Academy of Sciences

Article

Keywords:

Posted Date: October 23rd, 2026

DOI: https://doi.org/10.21203/rs.3.rs-11449021/v1

License: This work is licensed under a Creative Commons Attribution 4.0 International License.
Read Full License

Additional Declarations: No competing interests reported.

The roles of nonharmonic damping and spatial correlation of atomic movements in determining the amplitudes and attenuation frequencies of electro-optic coefficients

Mouyi Weng[1,*] and Lin-Wang Wang[1,†]

[1] *State Key Laboratory of Optoelectronic Materials and Devices, Institute of Semiconductors, Chinese Academy of Sciences, Beijing, China*

(Dated: September 10, 2026)

Abstract

Large electro-optic coefficients make ferroelectric materials attractive for high-speed optical modulation in optical communication. However, in materials like barium titanate this coefficient decreases markedly with increasing modulation frequency. This decrease can limit the bandwidth of electro-optic modulators, making it essential to understand the underlying attenuation mechanism. In this paper, we find that it is the nonharmonic damping of the phonon modes, instead of the phonon mode frequency itself, that plays an important role in determining both the amplitude of the low-frequency electro-optic coefficient and its attenuation frequency. Furthermore, we find that spatial correlations in atomic movements across many unit cells play an important role in determining both the static electro-optic coefficient and its attenuation frequency. We tested this hypothesis in tetragonal BaTiO3, where the electro-optic coefficient is experimentally well determined. Molecular-dynamics simulations using a machine-learned HSE potential give a low-frequency electro-optic coefficient of 590 pm/V and an attenuation frequency of approximately 137 GHz, both comparable to the experimental values.

* mouyiweng@semi.ac.cn

† lwwang@semi.ac.cn

INTRODUCTION

Electro-optic (EO) coefficient is defined as the change of optical dielectric constant when an electric field is applied to the bulk material. Large EO coefficient materials enable electrical control of light transmission in optical communication using an electro-optic modulator (also called Mach-Zehnder modulator) through interference between two branches of laser light with one subjected to a transverse electric signal. Finding materials with large EO coefficients and remaining constant at high electric signal frequency is thus an important task for optical communication. Barium titanate ($BaTiO_3$, BTO) combines large EO coefficients with demonstrated capability to be integrated into silicon photonics [1, 2], makes it an attractive material for high-speed optical communication. However, the measured EO coefficient decreases from approximately 480 pm/V at low frequency to 191 pm/V at 330 GHz, and even smaller at higher frequencies. This dispersion was described by a Debye-type relaxation model linked to the measured dielectric response, suggesting a connection to slow polarization dynamics [3]. This attenuation limits the modulation frequency, hence the optical communication band width. It is thus important to understand the underlying mechanism of this frequency dependent attenuation.

Current first-principles method can calculate the static EO tensor. They usually distinguish electronic, ionic, and piezoelectric contributions, with the ionic contribution, due to external electric field induced atomic displacements, often plays dominating roles in ferroelectric materials [4]. The ionic response is commonly evaluated as a sum over phonon modes, with each mode's contribution determined by its Raman tensor, Born effective charges, and frequency, while the entire calculation is based on the harmonic approximation [5, 6]. Previous calculations have linked large EO coefficients to soft polar phonon modes and ferroelectric instabilities [4, 7]. In tetragonal BTO, a low-frequency Raman-active mode has been identified as a major source of the large ionic response and is associated with a locally symmetry-broken configurations [8]. However, such harmonic phonon picture cannot describe the frequency attenuation behavior of EO coefficient. Even the soft optical phonon frequency is at several THz, much higher than the observed attenuation frequency.

Furthermore, the energy landscape and the related phonon mode for BTO is much more complicated. At 300K, BTO is a ferroelectric phase, with ferroelectric displacement defined as the z direction. For EO coefficient, the applied external electric field is at x or y direction.

In x and y direction, the experimental measured averaged atomic structure at 300K is at the high symmetry point. Room-temperature neutron scattering measurements further reveal strongly anisotropic soft-mode energies and damping in tetragonal $BaTiO_3$, with the lowest transverse optical branch along [110] reported to become overdamped near the Γ point [9]. However, harmonic DFT calculations at 0 K yield imaginary phonon frequencies for this experimentally observed tetragonal structure. Previous molecular dynamics simulations have revealed local Ti off-centering [10], motivating the construction of locally symmetry-broken structures for harmonic EO calculations [11].

Beyond first-principles calculations, effective-Hamiltonian molecular dynamics, Landau-type thermodynamic models, phase-field models and time-dependent Ginzburg–Landau models have been used to investigate polarization dynamics and electro-optic responses, with parameters obtained from first-principles calculations and experimental data. Effective-Hamiltonian molecular dynamics [12] and phenomenological models have provided important insights into polarization dynamics and EO responses in ferroelectrics. These approaches have reproduced dielectric relaxation, examined enhanced responses near phase transitions and domain walls, and modeled frequency-dependent EO behavior [13, 14]. However, the microscopic relationship between atomic movement correlations, the EO magnitude, and its attenuation frequency remains insufficiently understood. A Landau-type model coupling lattice and electronic polarizations has related the static EO coefficient to the lattice susceptibility [15]. Subsequent dynamical phase-field approaches have predicted enhanced EO responses near domain walls and during polarization switching in $BaTiO_3$ thin films [16]. However, the modulation-frequency dependence and characteristic relaxation frequencies of these contributions were not determined. Frequency-dependent EO coefficients have also been modeled using first-principles-derived Landau–Devonshire parameters combined with time-dependent Ginzburg–Landau dynamics [17]. However, this approach relies on an empirically specified kinetic coefficient and does not directly reproduce the modulation-frequency-dependent attenuation observed experimentally in $BaTiO_3$ [3].

As discussed above, the frequency dependence of the EO coefficient is often studied in connection with its ferroelectric behavior. In study the ferroelectricity of BTO, machine-learning potentials have reproduced the ferroelectric phase sequence of $BaTiO_3$ and enabled atomistic studies of its thermodynamics and dielectric properties [18]. Related machine-learned dipolar models have further enabled simulations of electric-field-driven nuclear dy-

namics in ferroelectric solids [19]. However, these approaches have not yet been applied to the EO coefficient or its frequency dependence.

In this study, we derive a theoretical relationship linking the low-frequency EO coefficient amplitude to spatial polarization correlations and their attenuation frequency. We find these EO property is highly related to the nonharmonic damping and the spatial atomic movement correlation of the phonon modes. In the overdamped regime, stronger spatial correlations produce a larger low-frequency EO coefficient and a lower attenuation frequency. To demonstrate this relationship in tetragonal BTO at 300 K, we constructed machine-learning potentials based on PBE and HSE DFT results and calculate the fixed-cell ionic EO coefficient using Green–Kubo molecular dynamics. The Green–Kubo PBE low-frequency EO coefficients agree with the Raman–Born mode sum evaluated using anharmonically renormalized phonon modes obtained from the stochastic self-consistent harmonic approximation (SSCHA) auxiliary force constants at 300 K. The HSE potential yields a low-frequency EO coefficient of approximately 590 pm/V and an attenuation frequency of approximately 137 GHz, close to the experimental values of 480 pm/V and 72.6 GHz respectively. Further analysis shows that the attenuation of the EO coefficient is governed by the spatially correlated dynamics of Ti ions, rather than by the dynamics of individual Ti ions, which has a much faster frequency.

RESULTS

Green–Kubo formulation of the static and dynamic EO coefficient

We calculate the fixed-cell ionic EO coefficient using the Green–Kubo formalism applied to molecular dynamics trajectories. Let $B_{ij} = (\boldsymbol{\varepsilon}^{\mathrm{opt}})^{-1}_{ij}$ denote the optical impermeability tensor and M_k the total dipole moment of the simulation cell. For classical nuclei, an external electric field couples to the dipole through $-E_k M_k$. The static response is then given by the equilibrium covariance [20]:

$$r^{\mathrm{ion}}_{ij,k}(0) = \left.\frac{\partial \langle B_{ij}\rangle}{\partial E_k}\right|_{\mathrm{ion}} = \frac{\langle \delta B_{ij}\, \delta M_k\rangle}{k_{\mathrm{B}} T}. \tag{1}$$

Here δB_{ij} and δM_k denote fluctuations on top of their equilibrium means, k subscript indicates the applied external electric field direction index.

To evaluate the optical and electrical observables, let $u_{a\alpha}$ denote the displacement of atom a from its equilibrium mean along Cartesian direction α. We retain the first-order observable expansions

$$\delta B_{ij} = \sum_{a\alpha} A_{ij,a\alpha} u_{a\alpha}, \qquad \delta M_k = e \sum_{b\beta} Z^*_{k,b\beta} u_{b\beta}. \tag{2}$$

Here a, b independently label all atoms in the simulation supercell, and $\alpha, \beta = x, y, z$ label Cartesian displacement directions. The coefficient $A_{ij,a\alpha} = (\partial B_{ij}/\partial u_{a\alpha})_0$ is the optical vertex obtained from the Raman tensor, and $Z^*_{k,b\beta} = e^{-1}(\partial M_k/\partial u_{b\beta})_0$ is the dimensionless Born effective charge, with e the elementary charge. The optical vertex is defined for the supercell-averaged impermeability. The conversion from primitive-cell tensors and the system-size normalization are detailed in SI Section S1 A.

Substituting Eq. (2) into Eq. (1) gives the static ionic EO coefficient,

$$r^{\mathrm{ion}}_{ij,k}(0) = \frac{e}{k_{\mathrm{B}}T} \sum_{a\alpha,b\beta} A_{ij,a\alpha} Z^*_{k,b\beta} \langle u_{a\alpha}(0) u_{b\beta}(0) \rangle. \tag{3}$$

The double sum includes both self correlations and cross correlations between different atoms and displacement directions. The zero in $r_(ij,k)^i on(0)$ indicates the frequency, while in $u_a\alpha(0)$, $u_b\beta(0)$ indicate the time. The frequency-dependent response follows from the Green–Kubo relation,

$$\begin{aligned} r^{\mathrm{ion}}_{ij,k}(\omega) = \frac{e}{k_{\mathrm{B}}T} \sum_{a\alpha,b\beta} A_{ij,a\alpha} Z^*_{k,b\beta} \Big[& \langle u_{a\alpha}(0) u_{b\beta}(0) \rangle \\ & + \mathrm{i}\omega \int_0^\infty \langle u_{a\alpha}(t) u_{b\beta}(0) \rangle e^{\mathrm{i}\omega t} \, \mathrm{d}t \Big]. \end{aligned} \tag{4}$$

All frequency-dependent ionic EO coefficients reported below are calculated using Eq. (4). Its zero-frequency limit recovers the static EO coefficient in Eq. (3), while the time evolution of the correlation function determines the frequency dependence. Both quantities are obtained directly from the MD trajectories, retaining anharmonic dynamics and all displacement cross correlations.

Effective collective-mode description of the static and dynamic response

To interpret the relation between response magnitude and attenuation frequency, we introduce an effective phonon-mode description. Let Q_ν denote an effective collective displacement coordinate with autocorrelation $C_\nu(t) = \langle Q_\nu(t) Q_\nu(0) \rangle$, and let $r_\nu(\omega)$ denote its

contribution to the EO response. Each coordinate is modeled using a linear restoring force and constant friction:

$$m_\nu \ddot{Q}_\nu(t) + \gamma_\nu \dot{Q}_\nu(t) + K_\nu Q_\nu(t) = \eta_\nu(t), \tag{5}$$

Here m_ν is the effective coordinate mass, and $\eta_\nu(t)$ is an equilibrium thermal random force. The effective friction γ_ν describes dissipative coupling to other modes. Its effects are implicitly included in the MD correlations; here it serves as an interpretive parameter and is not explicitly extracted from the trajectories. The effective stiffness $K_\nu = k_\mathrm{B}T/\langle Q_\nu^2 \rangle$ reproduces the variance sampled from MD. Multiplying by $Q_\nu(0)$ and using $\langle \eta_\nu(t) Q_\nu(0) \rangle = 0$ for $t > 0$ gives

$$m_\nu \ddot{C}_\nu(t) + \gamma_\nu \dot{C}_\nu(t) + K_\nu C_\nu(t) = 0. \tag{6}$$

The equilibrium conditions are $C_\nu(0) = \langle Q_\nu^2 \rangle$ and $\dot{C}_\nu(0) = 0$. Note, Q_ν is the effective phonon mode, hence related to the atomic displacement $u_a\alpha$ in the Green-Kubo formula. Taking a one-sided Fourier transform of Eq. (6) and substituting the independent-mode correlation sum into the Green–Kubo relation [Eq. (4)], as derived step by step in SI Section S1 C, gives the frequency-dependent contribution of Q_ν to the EO coefficient:

$$r_\nu(\omega) = r_\nu(0) \frac{\omega_{0,\nu}^2}{\omega_{0,\nu}^2 - \omega^2 - \mathrm{i}\Gamma_\nu \omega}. \tag{7}$$

Here $r_\nu(0) = R_{ij,\nu} Z_{k,\nu} C_\nu(0)/(k_\mathrm{B}T)$, $\omega_{0,\nu}^2 = K_\nu/m_\nu$, and $\Gamma_\nu = \gamma_\nu/m_\nu$. Note, Eq. (7) only considered one effective quasi phonon mode and its dissipation. If we assume $\langle Q_\mu(t) Q_\nu(0) \rangle = 0$ for different quasi-phonon mode, then Within this effective independent-mode description, the total EO coefficientresponse is

$$r_{ij,k}^{\mathrm{ion}}(\omega) = \sum_\nu r_{ij,k,\nu}^{\mathrm{ion}}(0) \frac{\omega_{0,\nu}^2}{\omega_{0,\nu}^2 - \omega^2 - \mathrm{i}\Gamma_\nu \omega}. \tag{8}$$

For a given quasi-phonon mode, if at modulation frequencies $|\omega| \ll \Gamma_\nu$, Eq. (7) reduces to the Debye form

$$r_\nu(\omega) \simeq \frac{r_\nu(0)}{1 - \mathrm{i}\omega\tau_\nu}, \tag{9}$$

where $\tau_\nu = \gamma_\nu/K_\nu$.

This equation is the Debye formula used in the experimental fitting of Ref. [3], with a characteristic attenuation frequency $f_D^\nu = (2\pi\tau_\nu)^{-1}$; which is centered at 72.6 GHz. But in the Debye fitting, only a single quasi-phonon mode is used. Using this Debye form, the

static EO contribution and the characteristic relaxation frequency can both be expressed in terms of the displacement variance $C_\nu(0)$:

$$r_\nu(0) = \frac{R_{ij,\nu} Z_{k,\nu} C_\nu(0)}{k_\mathrm{B} T}, \qquad f_D^\nu = \frac{k_\mathrm{B} T}{2\pi\gamma_\nu C_\nu(0)}. \tag{10}$$

Thus, for each independent coordinate in the overdamped limit,

$$r_\nu(0) f_D^\nu = \frac{R_{ij,\nu} Z_{k,\nu}}{2\pi\gamma_\nu}. \tag{11}$$

In this equation, the $C_\nu(0)$ has been cancelled, which means, for an overdamped mode, a larger displacement variance(e.g, due to the phonon softness, or a stronger coupling to the external electric field) increases the magnitude of its static EO amplitude, but it also lowers its attenuation frequency.

While the above analysis is based on the quasi-phonon modes, our Green–Kubo calculation evaluates the full EO coefficient from MD directly without resolving individual modes. The mode description above provides an interpretation of this response. In the following, we extract an effective Debye frequency $f_D = (2\pi\tau_D)^{-1}$ by fitting the calculated response to a Debye term and a constant background [Eq. (19)]. This fit separates the effective relaxing contribution from the background and provides a characteristic frequency for comparison with experiment, without assigning individual microscopic modes.

Intrinsic EO dispersion in $BaTiO_3$

We first investigate the fixed-cell ionic EO coefficient of tetragonal BTO at 300 K using static mode analysis, with $r_\mathrm{eff} = r_{42} + r_{13}/2$ used for comparison with experiment. The ideal tetragonal $P4mm$ reference structure exhibits imaginary soft phonon frequencies in 0 K harmonic calculations [11]. We therefore train a machine-learning potential on PBE reference data and use it to perform SSCHA calculations at 300 K [21, 22]. The phonon dispersion obtained from the mass-weighted SSCHA auxiliary force constants is shown in Fig. 1(a), with the modes characterized by their in-plane (xy) and out-of-plane (z) Ti displacement components. At the Γ point, the three acoustic modes are followed by the two lowest optical modes, $\nu = 4, 5$, which are degenerate at 3.75 THz and have strong Ti xy displacement character.

We then evaluate the contribution of each SSCHA mode to the static EO coefficient [Fig. 1(b)] by projecting the SSCHA eigenvectors at the Gamma point onto the Raman and

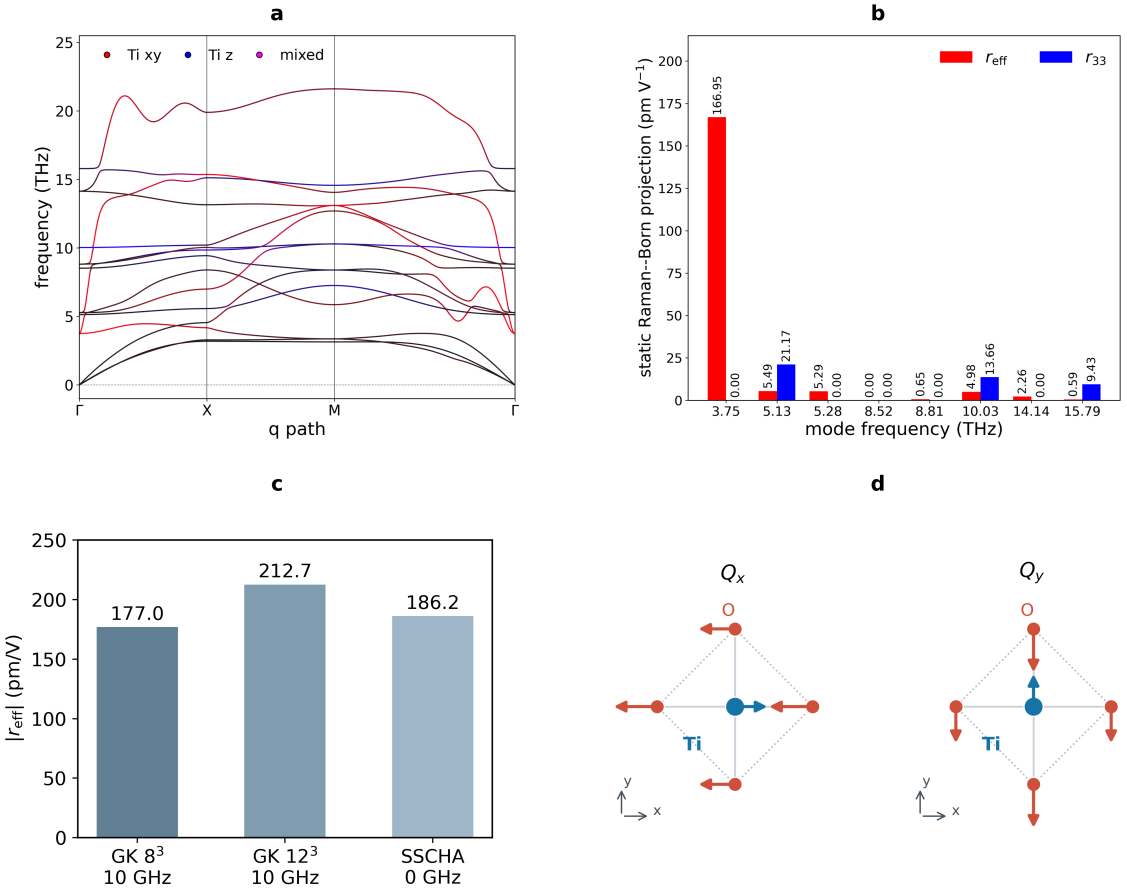

FIG. 1. **PBE EO coefficient and transverse soft modes at 300 K.** (a) Phonon dispersion from auxiliary SSCHA force constants at 300 K, colored by the xy-plane and z-direction components of the Ti displacement relative to its O_6 cage. The two color weights are normalized separately within this panel. (b) Grouped static ionic Raman–Born contributions to r_{eff} and r_{33} for the same $8 \times 8 \times 8$ auxiliary reference. (c) Green–Kubo (GK) $|r_{\mathrm{eff}}(10\ \mathrm{GHz})|$ for PBE 8^3 and 12^3 supercells, compared with the static ionic SSCHA mode-sum value of 186.2 pm/V, electronic and strain-mediated piezoelectric contributions are excluded. (d) Atomic displacement patterns of the two lowest-frequency optical phonon modes at Γ obtained from SSCHA calculations. Both modes have a frequency of 3.75 THz and are polarized in the xy plane, shown here in an x/y basis. Blue and red arrows indicate Ti and equatorial O displacements, respectively; Ba and apical O are omitted for clarity.

Born channels and combining these projections with the inverse restoring stiffnesses from the SSCHA auxiliary force constants. The static Raman–Born mode sum is given in Eq. (18), with its normalization derived in SI Section S1 B. This gives an independent static reference with approximate anharmonic renormalization. The two lowest-frequency optical branches at Γ, with frequency 3.75 THz, together contribute 166.95 pm/V, accounting for 89.7% of the static ionic r_{eff}. The dominant quasi-mode displacement pattern is the in-plane motion in the xy plane of Ti relative to its O_6 octahedral cage, with Ti and the neighboring oxygen atoms moving in opposite directions. Within this degenerate pair, the modes can be chosen as an x-polarized and a y-polarized partner, as illustrated in Fig. 1(d).

To make this microscopic connection explicit, we next explain how this in-plane mode contributes to r_{42}, i.e., how a field along y produces the yz component of the static EO coefficient. For a field along y, the y-polarized partner contributes through $r_{42} = r_{yz,y}$: an applied E_y couples most strongly to this mode through its electrical projection $Z_{y,\nu}$, the mode displacement then changes the off-diagonal susceptibility element ϵ_{yz} through the Raman derivative $R_{yz,\nu}$, and this Raman–Born product builds the mode contribution to $r_{yz,y}$. By tetragonal symmetry, the same argument applies to the x-polarized partner for $r_{51} = r_{zx,x}$ under exchange of x and y. Here $r_\nu(0)$ denotes an individual mode contribution, while the numerical comparisons retain the full r_{eff}.

The PBE SSCHA finite-temperature phonons and Raman–Born mode sum provide a static ionic reference of 186.2 pm/V. Figure 1(c) compares this value with the Green–Kubo magnitudes at 10 GHz for 8^3 and 12^3 supercells: 177.0 and 212.7 pm/V, respectively. The Green–Kubo values use 0.15 ns segment complex means. They sample the low-frequency plateau rather than the exact zero-frequency limit. The two values bracket the SSCHA reference and support agreement between the approaches at low frequency. The mode decomposition identifies the transverse soft-mode sector as the dominant contribution to the PBE response.

We next turn to the frequency dependence of the EO coefficient. Dynamic Green–Kubo calculations with the PBE potential for 8^3 and 12^3 supercells show EO dispersion on the THz scale [Fig. 2(a)]. These PBE spectra are compared directly; we do not assign them a single-Debye frequency because this model does not adequately describe their complex THz response over the tested intervals. We next use an HSE-based machine-learning interatomic force field and calculate the modulation-frequency-dependent EO coefficient within the same

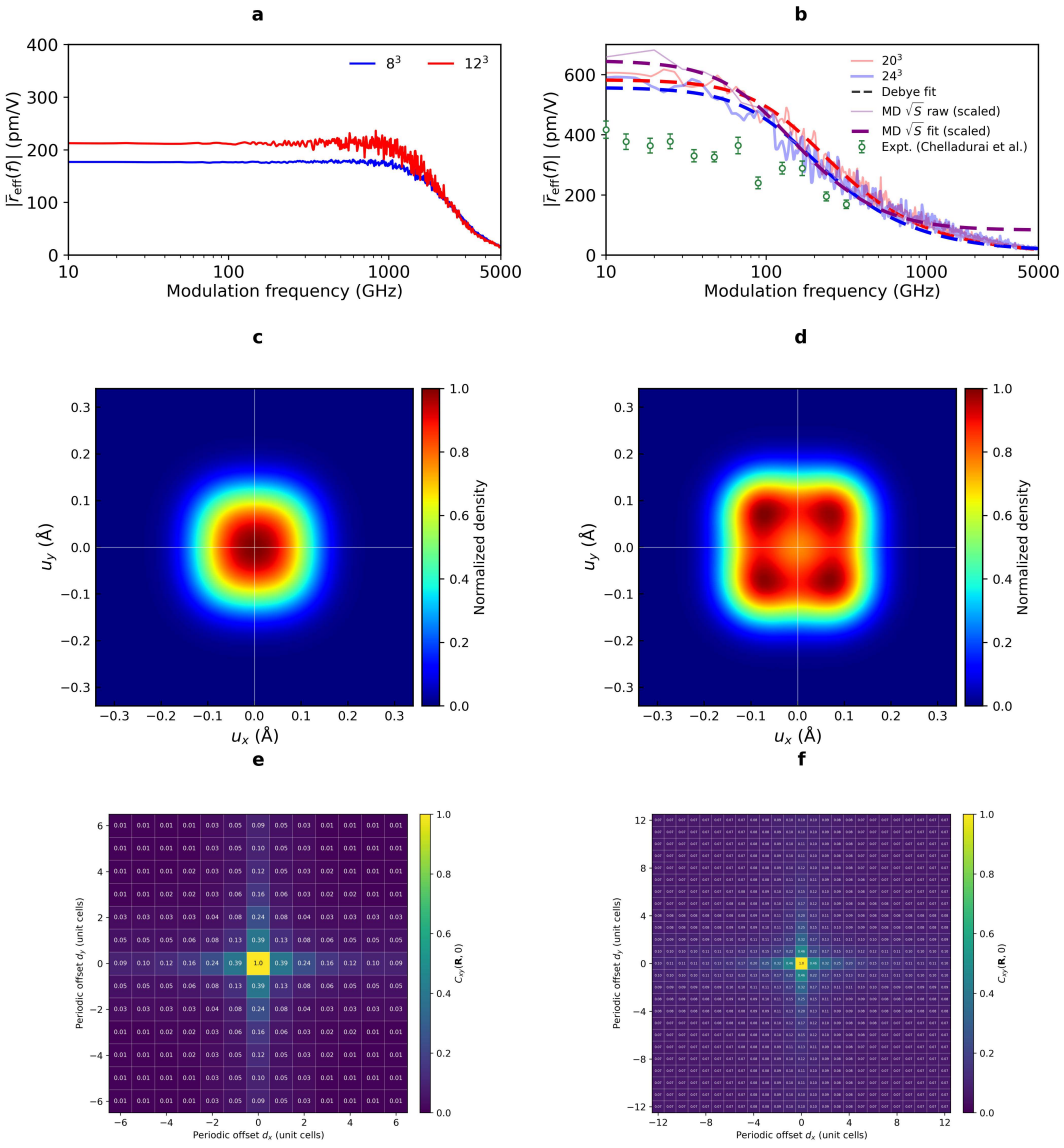

FIG. 2. **EO spectra and Ti displacement correlations at 300 K.** (a,b) Complex-mean EO magnitudes for PBE (8^3, 12^3) and HSE (20^3, 24^3). Red/blue dashes in (b): Debye fits, $f_D = 158.67/137.15$ GHz for $20^3/24^3$. Purple curves show $|r_{\rm eff}^{24^3}(100)|\sqrt{S(f)/\overline{S}(100)}$ using raw 100 GHz normalization. Scaling is for display only. Green circles: experimental $\frac{1}{2}(r_{13}+2r_{42})$ from Ref. [3], with two-standard-error bars. (c,d) In-plane Ti displacement distributions relative to the oxygen cage for PBE (12^3) and HSE (24^3), respectively. Each distribution is normalized by its own maximum. (e,f) Normalized equal-time same-layer $C_{xy}(\boldsymbol{R}, 0)$ for PBE (12^3) and HSE (24^3), on the same color scale.

TABLE I. HSE EO coefficient magnitude at 10 GHz and attenuation frequency f_D versus cubic supercell size at 300 K.

Replication grid	$\lvert r_{\mathrm{eff}}(10\ \mathrm{GHz})\rvert$ (pm/V)	f_D (GHz)
8^3	471.3	240.11
12^3	704.1	169.81
16^3	706.9	148.82
20^3	606.2	158.67
24^3	590.2	137.15

dynamic Green–Kubo framework [Fig. 2(b)]. A comparison of HSE 8^3, 12^3, 16^3, 20^3, and 24^3 spectra using the same 0.15 ns segment duration is shown in SI Fig. S1. For the HSE 12^3, 16^3, 20^3, and 24^3 cells, the values of $|r_{\mathrm{eff}}(10\ \mathrm{GHz})|$ are 704.1, 706.9, 606.2, and 590.2 pm/V, respectively (Table I). Taken together, these results place the low-frequency HSE EO coefficient at approximately 600 pm/V for the largest cells considered.

We extract f_D from the HSE complex response over 25–5000 GHz with equal weights for the real and imaginary residuals [Eq. (19)]. For the 12^3, 16^3, 20^3, and 24^3 cells, the fitted f_D values are 169.81, 148.82, 158.67, and 137.15 GHz, respectively (Table I). The largest-cell result corresponds to $\tau_D = 1.16$ ps. Although some finite-size dependence remains, the largest-cell results establish a characteristic attenuation frequency of order 10^2 GHz, comparable to the experimental relaxation scale [3]. A 24^3 $BaTiO_3$ supercell contains 69,120 atoms, making further size and sampling tests computationally demanding even with the NEP force field. The complex spectra and matching fits are shown in SI Section S7. It is worth mentioning that the attenuation emerges in fixed-cell, single-domain simulations without domain walls, demonstrating that collective lattice dynamics alone can produce substantial EO dispersion.

To examine the EO attenuation from a phonon-mode perspective, we extract two dominant collective displacement coordinates from the HSE 24^3 MD trajectories by diagonalizing the mass-weighted displacement covariance, as the HSE SSCHA calculations did not converge satisfactorily due to the strongly non-Gaussian Ti displacement distributions. Their subspace closely matches the two lowest-frequency optical modes at Γ (modes 4 and 5) obtained from the PBE SSCHA calculations, whose displacement patterns are illustrated in

Fig. 1(d).

We then calculate the frequency spectra of the MD displacements projected onto these two MD covariance coordinates. In the overdamped regime, the square root of the normalized displacement spectrum has the same frequency dependence as the normalized EO contribution of the corresponding mode [Eq. (9)]. Figure 2(b) compares the square root of the normalized mean displacement spectrum with the full EO magnitude calculated using the Green–Kubo formalism. Fitting the mean displacement spectrum to a Lorentzian relaxation term plus a constant background gives approximately 104 GHz, corresponding to a relaxation time of 1.53 ps, compared with 137 GHz from the complex EO response (SI Section S8). The close agreement between the normalized curves suggests that these two modes dominate the EO attenuation in the HSE calculations and supports our phonon-mode description of the frequency-dependent EO response.

It is worth noting that, in the overdamped regime, the frequency response reduces to the Debye form in Eq. (9), whose frequency dependence is determined solely by the relaxation time τ_ν (or equivalently f_D^ν). Therefore, the characteristic phonon frequency $\omega_{0,\nu}$ and friction coefficient γ_ν cannot be independently determined from the MD spectra in this regime.

To have a deeper understanding of the atomic dynamics of the system, we examine the spatial correlation of the atomic displacements, focusing on the in-plane motion of Ti. Figures 2(c) and 2(d) show the MD trajectory averaged xy-plane projection of the Ti off-centering relative to its O_6 octahedral cage for PBE and HSE, respectively. The PBE distribution is concentrated around the center without significant off-centering, whereas HSE clearly resolves four distinct off-centered regions. Consistent with this more strongly localized anharmonic landscape, the free-energy surface extracted from the MD trajectories exhibits significant barriers in HSE: the nearest-neighbor barrier is 5.40 meV in HSE, while the through-center barrier is 12.1 meV.

Figures 2(e) and 2(f) show the same-layer xy-displacement correlations for PBE and HSE in their respective MD trajectories. We use normalized displacement correlations to compare the relative collective alignment of Ti displacements in PBE and HSE. The HSE potential produces more pronounced Ti off-centering and substantially longer-ranged in-plane displacement correlations than PBE. For example, along the in-plane lattice axis, the normalized correlation at a separation of six unit cells is approximately 0.15 for HSE, compared with 0.09 for PBE. The difference is even more pronounced along the diagonal,

indicating that HSE stabilizes collective polarization fluctuations over a larger spatial range.

Besides the time correlation function in analysize the attenuation frequency, we also like to study the spatial correlation function of the atomic movement. One of the reasons is that, the BTO is a ferroelectric material, even in the x-y plane, the atomic energy potential surface is highly nonharmonic, it has a negative curvature at the high symmetry point. There are speculations that the large EO coefficient is related to its ferroelectric behavior and the attenuation frequency might be related to the ferroelectric flipping. The atomic movement behavior of a ferroelectric material is very different from the pure phonon mode behavior of a harmonic system. The polarization of a ferroelectric material is a long range order which does not decay with the distance. In the x-y plane, if the temperature further drop, it is also a ferroelectric material. Room temperature is above this transition temperature, but nevertheless, its atomic movement spatial correlation can have a much longer range than a pure harmonic system. To study this, we examine the Ti–Ti force response to a displacement of a neighboring Ti atom. We project the force response of the central Ti onto the Ti–Ti separation direction, so that a positive $\beta_{\parallel}^{xy}$ indicates a cooperative tendency for neighboring Ti displacements to align in the same direction. HSE systematically strengthens this cooperative response relative to PBE over several coordination shells (SI Table S1). For the nearest-neighbor [100] pair, $\beta_{\parallel}^{xy}$ increases from 6.71 to 7.24 eV/Å^2, corresponding to a 7.8% enhancement from PBE to HSE. The enhancement becomes even more pronounced for more distant neighbors: from 0.245 to 0.296 eV/Å^2 for the [111] shell, from 0.107 to 0.147 eV/Å^2 for [211], and from 0.0430 to 0.0700 eV/Å^2 for [220]. All these $\beta_{\parallel}^{xy}$ values are significantly larger than the long-range interaction [23] described in the Methods section, which has a characteristic magnitude of only $\sim 10^{-3}$ $eV/\mathring{A}^2$. This longer range interaction has been attributed to the following fact: the Ti–O orbital hybridization gives rise to anomalously large dynamical charges and enhances the dipole–dipole interaction that favors correlated Ti displacements [4]. The usually longer correlation might have contributed to the large EO coefficient.

Correlation-controlled EO coefficient magnitude and attenuation

To establish the role of collective displacement correlations, we perform two controlled numerical tests. First, we vary the short-range interactions at fixed supercell geometry to

modify the strength of polarization correlations. Second, we vary the lateral supercell size at fixed interactions to constrain their spatial extent. Figure 3 compares the resulting EO magnitude, attenuation frequency, and amplitude–frequency product.

We first vary the short-range interaction while keeping the supercell geometry fixed, together with the same Born–LR term and fixed optical and electrical vertices:

$$U_\lambda = (1-\lambda)U_{\mathrm{PBE}}^{\mathrm{SR}} + \lambda U_{\mathrm{HSE}}^{\mathrm{SR}} + U_{\mathrm{LR}}. \tag{12}$$

Here $\lambda = 0$ and 1 correspond to the PBE and HSE endpoints, whereas $\lambda = 1.5$ and 2 extrapolate the short-range difference beyond HSE. As λ increases from 0 to 1, 1.5, and 2, the nearest-neighbor correlation rises from 0.406 to 0.500, 0.572, and 0.633 [Fig. 3(c)]. As the correlation increases, the coherent 10 GHz effective EO coefficient increases from 196 to 509, 1056, and 1635 pm/V. For $\lambda = 0$, 1, 1.5, and 2, the common 25–5000 GHz fits give attenuation frequencies of 1211.59, 220.05, 56.53, and 20.41 GHz, respectively [Fig. 3(a,b)]. The fitted f_D for $\lambda = 2$ lies slightly below the fitting range and should therefore be regarded as an extrapolated estimate. The PBE endpoint is summarized by an effective single-Debye parameter; its complex spectrum and fit are shown alongside HSE in SI Fig. S3. The HSE-to-$\lambda = 2$ comparison supports enhanced low-frequency response and slower attenuation as the short-range cooperative interaction is strengthened. Methods and SI Table S2 document the fitting protocol and data coverage.

In the second test, we keep the HSE interaction and Raman–Born vertices fixed and progressively truncate the lateral dimensions from the largest-cell with $N_z = 4$ and $N_x = N_y$ reducing from 24 to 6. We keep $N_z = 4$ so that the layer-resolved correlation contributions remain positive within the retained thickness; for larger N_z, positive correlations near $\Delta z = 0$ are partially cancelled by negative contributions from more distant layers (SI Fig. S2). The lateral truncation therefore provides a controlled way to reduce the spatial extent of the collective correlation field without introducing such sign cancellations, while leaving the local cooperative interaction unchanged.

As the spatial constraint is relaxed from the smallest to the largest cell, the low-frequency effective EO coefficient increases from 328 to 2465 pm/V, while f_D decreases from 313.73 to 47.38 GHz [Fig. 3(a,b)]. Over the same sequence, the nearest-neighbor correlation remains nearly unchanged, varying only from 0.498 to 0.505 [Fig. 3(c) and SI Table S3]. Despite nearly unchanged nearest-neighbor correlations, increasing the lateral supercell size substan-

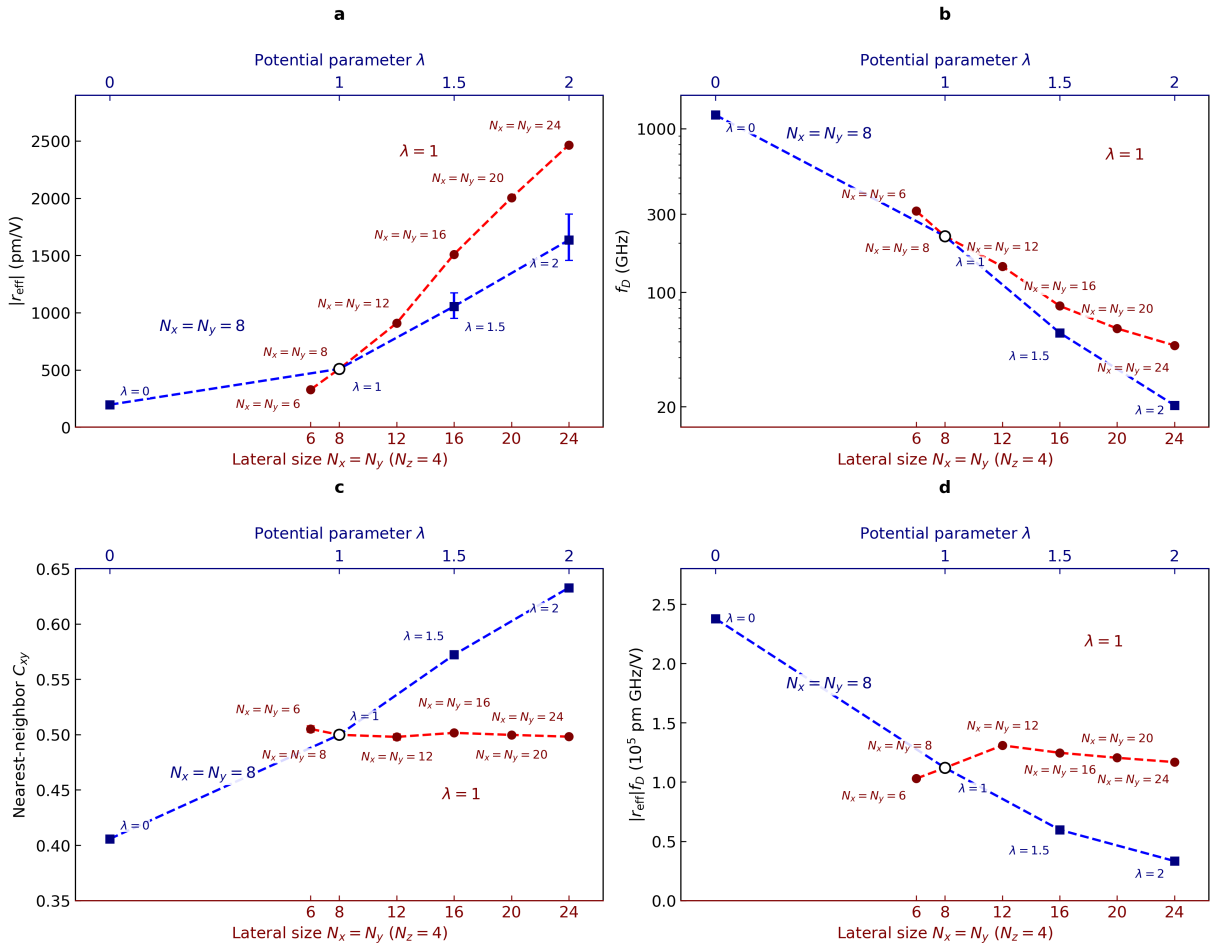

FIG. 3. **Effects of lateral size and short-range interactions on the EO coefficient.** Red circles use the lower axis: HSE cells with $N_x = N_y$ and $N_z = 4$. Blue squares use the upper axis: varying λ at fixed $8 \times 8 \times 4$ geometry. (a) $|r_{\text{eff}}|$ evaluated at 10 GHz for both series. The curves use 0.15 ns segments where available; the $24 \times 24 \times 4$, $\lambda = 1.5$, and $\lambda = 2$ points retain full-current data (SI Section S7). (b) Attenuation frequency f_D. The PBE endpoint ($\lambda = 0$) uses the same fit interval and weighting. (c) Normalized same-layer nearest-neighbor correlation $C_{xy}(a\hat{\boldsymbol{x}}, 0)$. (d) Product of the amplitudes in (a) and frequencies in (b). The HSE $8 \times 8 \times 4$ point ($\lambda = 1$) is shared by both series and marked by an open black circle; it aligns the two horizontal axes. Point labels identify the varying parameter.

tially enhances the low-frequency EO coefficient and lowers its attenuation frequency. This demonstrates that local alignment alone is insufficient to explain the response; the spatial extent of collective correlations is also essential.

The amplitude–frequency products further distinguish the two controls. For the spatial-truncation series, once $N_x = N_y \geq 12$, the product remains within 1.17×10^5–1.31×10^5 pm GHz/V [Fig. 3(d)]. This approximate compensation between the increase in EO coefficient magnitude and the decrease in f_D is consistent with Eq. (11) when the dominant soft contribution has fixed projected Raman and Born vertices and an approximately unchanged displacement friction. Thus, when the interaction is fixed and only the spatial correlation is constrained, the amplitude–frequency relation is close to the constant-parameter predicted by Eq. (11).

The first test with changed short-range interaction behaves differently: the product decreases from 2.38×10^5 at $\lambda = 0$ to 1.12×10^5 at $\lambda = 1$, 5.97×10^4 at $\lambda = 1.5$, and 3.34×10^4 pm GHz/V at $\lambda = 2$ [Fig. 3(d)]. Unlike the spatial-truncation series, changing the interaction potential does not preserve the effective dynamical parameters entering Eq. (11), so a constant amplitude–frequency product is not expected. Compared with PBE, HSE exhibits more pronounced Ti off-centering in Fig. 2(c,d), indicating a more strongly anharmonic effective free-energy landscape, together with a lower characteristic EO attenuation frequency.

DISCUSSION

Ferroelectric order and the static EO coefficient

To connect spontaneous polarization in the ferroelectric phase with correlations between collective atomic displacements, we can write the full polar coordinate at temperature T as

$$\mathcal{Q}_\nu(t;T) = \overline{\mathcal{Q}}_\nu(T) + Q_\nu(t;T), \qquad \langle Q_\nu(t;T)\rangle_T = 0. \tag{13}$$

Here Q_ν retains its definition from the preceding theory, and $\overline{\mathcal{Q}}_\nu(T)$ is the mean distortion relative to the chosen nonpolar reference. For a coordinate associated with spontaneous polar order, $\overline{\mathcal{Q}}_\nu(T)$ is nonzero below T_c in a selected ferroelectric domain and vanishes above T_c in the paraelectric phase. Within the linear Born-charge approximation, its contribution

to the spontaneous polarization is

$$P^{\mathrm{s}}_{k,\nu}(T) \simeq \frac{Z_{k,\nu}}{V(T)} \overline{\mathcal{Q}}_\nu(T). \tag{14}$$

The corresponding connected variance is

$$C_\nu(0;T) = \begin{cases} \langle \mathcal{Q}^2_\nu \rangle_T - \overline{\mathcal{Q}}^2_\nu(T), & T < T_c, \\ \langle \mathcal{Q}^2_\nu \rangle_T, & T > T_c. \end{cases} \tag{15}$$

In an order–disorder picture, heating through T_c makes the average polar displacement vanish, $\overline{\mathcal{Q}}_\nu(T > T_c) = 0$, while individual atoms can still be displaced from their average positions.

The temperature dependence of this variance can be illustrated by combining the equilibrium fluctuation–response relation with the susceptibility scaling near a continuous ordering transition [24]. For the collective coordinate associated with the transition, approaching from the disordered side,

$$\langle \mathcal{Q}^2_\nu \rangle_T \propto k_{\mathrm{B}} T \left| \frac{T - T_c}{T_c} \right|^{-\gamma_{\mathrm{c}}}, \tag{16}$$

where $\gamma_{\mathrm{c}} > 0$ is the static susceptibility exponent. For a continuous ordering transition, the connected polarization fluctuations can grow strongly on approaching the transition temperature from above, as reflected in the critical scaling of the susceptibility. This illustrates how large collective fluctuations can persist even in the absence of long-range polar order.

Tetragonal BTO illustrates how these conditions can coexist. At 300 K, ferroelectric order along z breaks inversion symmetry and allows a nonzero Raman coupling $R_{yz,\nu}$ for the y-polarized transverse mode. Meanwhile, the xy-plane Ti–O displacements remain disordered, with zero mean but strong collective correlations in the xy plane. Retaining the dominant transverse soft-mode pair gives the approximate static contribution

$$r^{\mathrm{ion}}_{42}(0) \simeq \frac{1}{k_{\mathrm{B}} T} \sum_{\nu=4,5} R_{yz,\nu} Z_{y,\nu} C_\nu(0). \tag{17}$$

Thus, the large r_{42} combines two effects: ferroelectric order along z enables the Raman coupling, while strong transverse displacement fluctuations provide a large $C_\nu(0)$. This microscopic picture is consistent with the thermodynamic interpretation of the enhanced transverse EO coefficient by Ross et al. [15].

Implications for EO materials design

Our calculation connects the ionic EO response magnitude and attenuation frequency to atomic movement correlations and their relaxation. These results suggest three considerations for EO materials design.

(1) Combining polar order with correlated transverse fluctuations.

Ferroelectric order can break symmetry and enable Raman coupling for polar modes [5, 6]. Meanwhile, strongly correlated transverse polarization fluctuations can persist without long-range order, particularly near a ferroelectric phase transition. Tetragonal BTO combines these features through polar order along z and correlated displacements in the xy plane. This suggests seeking materials that combine polar order along one direction with soft, strongly correlated fluctuations along the transverse directions.

(2) Reducing friction to extend the EO bandwidth.

In the overdamped regime, the attenuation frequency is given by $f_D^\nu = K_\nu/(2\pi\gamma_\nu)$, indicating that reducing the effective friction γ_ν can increase f_D^ν without sacrificing the static EO coefficient. Defects and interfaces can introduce additional dissipation and relaxation channels [25], suggesting that minimizing these extrinsic effects may help preserve the EO response at higher frequencies.

(3) Balancing EO magnitude and attenuation frequency.

Stronger atomic movement correlation $C_\nu(0)$, enhance the static EO coefficient but reduce the attenuation frequency f_D^ν. This trade-off is reflected in the amplitude–bandwidth product, $|r_\nu(0)|f_D^\nu = |R_{ij,\nu}Z_{k,\nu}|/(2\pi\gamma_\nu)$, which is independent of $C_\nu(0)$. Tuning collective polarization correlations through temperature or epitaxial strain may therefore provide a practical route to optimize the balance between EO magnitude and attenuation frequency for specific device requirements.

METHODS

First-principles calculations and molecular dynamics

Exchange and correlation are described using the Perdew–Burke–Ernzerhof (PBE) generalized-gradient approximation [26] and the Heyd–Scuseria–Ernzerhof (HSE) screened hybrid functional [27].

The static Born effective-charge and Raman tensors defining the fixed reference vertices were calculated with the plane-wave DFT code QUANTUM ESPRESSO [28, 29], orchestrated by the AiiDA workflow manager [30, 31]. Polarization finite differences were evaluated with AiiDA-vibroscopy [32], within the modern theory of polarization [33] and the electric-enthalpy formalism [34, 35]. Norm-conserving SG15 pseudopotentials were used [36–38]. The common tetragonal reference has $a = 3.98$ Å, $c = 4.11$ Å, and volume 65.1 Å^3. The PBE/HSE tensor audits use 70 Ry and 280 Ry wave-function and charge-density cutoffs, a Gamma-centered $4 \times 4 \times 4$ mesh, electronic threshold 5×10^{-10}, and a 0.010 Åcentral displacement. HSE uses 25% exact exchange and screening parameter 0.106.

The finite-temperature PBE reference in Fig. 1(a–c) was obtained with the stochastic self-consistent harmonic approximation (SSCHA), following the variational anharmonic framework of Monacelli et al. [21]. The PBE-NEP potential with the Born–LR correction was sampled at 300 K in an $8 \times 8 \times 8$ supercell with 75 irreducible wave vectors. Each population contained 40,000 configurations with positive–negative paired sampling; the auxiliary second-order force constants converged in the third population. The frequencies and eigenvectors used here are those of these auxiliary force constants. Mode colors represent the Ti displacement relative to the average displacement of its six nearest oxygen neighbors, including the wave-vector-dependent phases for periodic images; the in-plane and out-of-plane squared amplitudes are normalized separately. The EO mode sum instead uses the zone-center frequencies and eigenvectors read directly from the auxiliary dynamical matrix. The static ionic EO reference in Fig. 1(c) was evaluated from the Raman–Born mode sum

$$
\begin{aligned}
r_{ij,k}^{\mathrm{ion,SSCHA}}(0) &= \sum_{\nu \in \Gamma\,\mathrm{opt}} r_{ij,k,\nu}^{\mathrm{ion}}(0), \\
r_{ij,k,\nu}^{\mathrm{ion}}(0) &= -e \sum_{ab} B_{ia} \left[\sum_{\kappa\alpha,\kappa'\beta} \frac{R_{\kappa\alpha,ab} Z^{*}_{k,\kappa'\beta} e_{\kappa\alpha,\nu} e_{\kappa'\beta,\nu}}{\sqrt{M_\kappa M_{\kappa'}}\,\Omega_\nu^2} \right] B_{bj}.
\end{aligned}
\tag{18}
$$

Here $B = (\boldsymbol{\varepsilon}^{\mathrm{opt}})^{-1}$, $R_{\kappa\alpha,ab} = \partial \varepsilon_{ab}^{\mathrm{opt}} / \partial u_{\kappa\alpha}$ is the atomic Raman tensor, $Z^{*}_{k,\kappa\alpha}$ is the dimensionless Born effective charge, and M_κ is the atomic mass. The indices κ, κ' label primitive-cell atoms, while a, b, α, β label Cartesian components; the prefactor e is the elementary charge. The normalized eigenvectors $e_{\kappa\alpha,\nu}$ and eigenvalues Ω_ν^2 are obtained from the mass-weighted auxiliary SSCHA dynamical matrix at 300 K, with $\sum_{\kappa\alpha} e_{\kappa\alpha,\nu} e_{\kappa\alpha,\mu} = \delta_{\nu\mu}$. The fixed reference Raman and Born tensors are projected onto these modes, and the sum runs over zone-center optical modes, excluding rigid translations. The plotted reference

is $r_{\mathrm{eff}}^{\mathrm{ion,SSCHA}}(0) = r_{yz,y}^{\mathrm{ion,SSCHA}}(0) + \frac{1}{2} r_{xx,z}^{\mathrm{ion,SSCHA}}(0)$, corresponding to $r_{42} + r_{13}/2$. The coordinate normalization and atomic-tensor projections are given in SI Section S1 B. The restoring stiffnesses in that projection are those of the SSCHA auxiliary force constants. Degenerate optical modes within 10^{-4} THz are grouped in Fig. 1(b), retaining signed contributions. Only the ionic contribution is plotted in Fig. 1(b,c): the electronic r_{eff} contribution of 1.6845 pm/V is excluded.

The PBE and HSE energies and forces used to construct the force data were evaluated with the GPU-accelerated plane-wave pseudopotential code PWmat [39, 40], using the same norm-conserving SG15 pseudopotentials. To construct efficient machine-learning potentials, representative configurations were first selected from the PBE molecular-dynamics trajectories in $4\times4\times4$ supercells (320 atoms) by feature-space reduction and stratified coverage [41]. This concentrates the expensive HSE-DFT calculations on a compact, representative training set; related MACE-assisted workflows have shown that system-specific potentials can be developed with only a few hundred additional ab initio configurations [42]. A MACE-based model was trained on 500 HSE-labelled configurations [43, 44]. This model was then used to generate force data for 10,000 representative frames selected from these $4 \times 4 \times 4$ PBE trajectories using the same feature-space reduction and stratified coverage procedure. These force data were used to train a neuroevolution potential (NEP) [45, 46]. In $4 \times 4 \times 4$ supercells, the PBE and HSE Ti displacement distributions have similar spatial coverage (SI Fig. S5). NEP was used for the long production trajectories because its inference is faster; its accuracy is more sensitive to training-set size and configuration coverage, motivating the MACE-generated expansion before production. The independent validation set contains 59 HSE-labelled 320-atom structures and is separate from the production trajectories. The force-component RMSE is 21.86 meV/Å for the short-range model and 21.34 meV/Å with Born–LR (SI Table S4).

The analytic Born–LR force uses fixed Born effective-charge tensors and the electronic dielectric tensor $\epsilon_\infty = \mathrm{diag}(5.473401, 5.473401, 4.848706)$ of the tetragonal reference structure. This type of long-range electrostatic construction has been shown to reproduce the LO–TO splitting and long-wavelength phonon dispersion of polar materials, including cubic $BaTiO_3$, from first-principles dielectric tensors and Born charges [23]. The $\boldsymbol{k} = 0$ vector is omitted. Training labels are $E_{\mathrm{short}} = E_{\mathrm{DFT}} - E_{\mathrm{LR}}$ and $\boldsymbol{F}_{\mathrm{short}} = \boldsymbol{F}_{\mathrm{DFT}} - \boldsymbol{F}_{\mathrm{LR}}$; production adds the same Born–LR term once.

The common protocol uses a 2 fs integration step, 100 ps Nose–Hoover-chain NVT equilibration with a thermostat coupling time of 100 fs, followed by NVE production under three-dimensional periodic boundaries. Velocities are initialized at 300 K, and stationary momentum is removed. Correlations use trajectory-wise mean removal, overlapping-sample normalization, a one-sided cosine taper, trapezoid integration, a retained equal-time contact term, and zero padding sufficient to avoid circular convolution. For the retained amplitude confidence intervals, independent trajectories were resampled with the archived trajectory-bootstrap procedure; complex EO coefficients are averaged coherently before taking the magnitude.

For both controls in Fig. 3, nearest-neighbor correlations are evaluated at $\boldsymbol{R} = a\hat{\boldsymbol{x}}$, with standard errors estimated across trajectories. The updated $\lambda = 2$ spectrum covers 10–5000 GHz and averages 16 full trajectories (3.0–3.4 ns) sampled every 50 fs.

Spectral analysis and relaxation fitting

To summarize attenuation, we fit the effective EO coefficient using the single-Debye form

$$r_{\mathrm{eff}}(\omega) \simeq r_{\mathrm{eff},\infty} + \frac{r_{\mathrm{eff},0} - r_{\mathrm{eff},\infty}}{1 - \mathrm{i}\omega\tau_D}, \qquad f_D = (2\pi\tau_D)^{-1}, \tag{19}$$

with $\omega = 2\pi f$. Fast contributions satisfying $|\omega\tau_\nu| \ll 1$ over the fit interval form an approximately constant background, while the slow response is summarized by one effective relaxation time. Here $r_{\mathrm{eff},0}$ is the fitted zero-frequency value, and $r_{\mathrm{eff},\infty}$ is the background relative to this slow relaxation. The difference $r_{\mathrm{eff},0} - r_{\mathrm{eff},\infty}$ is the fitted relaxation amplitude.

Complex EO coefficients were averaged within each trajectory and then equally across trajectories before taking the magnitude. We fit $\mathrm{Re}\, r_{\mathrm{eff}}$ and $\mathrm{Im}\, r_{\mathrm{eff}}$ jointly by least squares on the supplied logarithmic frequency grid, with real background and residue and $f_D > 0$. We use 0.15 ns segment complex means wherever available, from 12 trajectories per cell, sampled every 2 fs. The fitted frequencies and products are shown as point estimates in Fig. 3. SI Tables S2 and S3 give available amplitude confidence intervals.

We analyze the zone-center collective displacement fluctuations of the HSE $24 \times 24 \times 24$ supercell at 300 K using twelve independent trajectories, each with 500 ps of analyzed dynamics sampled every 2 fs. Mass-weighted displacements of the five atomic sublattices define a 15-dimensional Cartesian coordinate space. We diagonalize the MD displacement

covariance and project the displacement trajectories onto its two leading orthogonal eigenvectors. These collective coordinates are obtained directly from MD, without selecting SSCHA modes. The PBE SSCHA eigenvectors are used only for a subsequent comparison of displacement subspaces, reported in SI Section S8.

For each projected coordinate, the displacement power spectral density is $S_\nu(f) = 2\,\mathrm{Re}\int_0^\infty C_\nu(t)e^{\mathrm{i}2\pi ft}\,\mathrm{d}t$, where $C_\nu(t) = \langle \delta Q_\nu(t)\delta Q_\nu(0)\rangle$. The spectra are estimated using 100 ps Hann-window Welch spectra and averaged across the twelve trajectories. We form the arithmetic mean $\overline{S} = (S_1 + S_2)/2$, which is invariant under orthogonal rotations within this two-dimensional subspace. The overall positive-frequency PSD convention does not affect normalized spectra or fitted relaxation frequencies.

We fit each coordinate spectrum and their mean to a Lorentzian relaxation term plus a constant background,

$$S_{\mathrm{fit}}(f) = B + \frac{A}{1 + (f/f_D)^2}, \tag{20}$$

with free real parameters A and B and $f_D > 0$. The effective relaxation time is obtained as $\tau = (2\pi f_D)^{-1}$.

DATA AVAILABILITY

The numerical data supporting the figures and analyses in this article and its Supplementary Information are publicly available in the Materials Cloud Archive at https://doi.org/10.24435/materialscloud:yh-wt. The deposit includes electro-optic spectra and Debye-fit results, Ti-displacement correlations, collective-mode spectra, SSCHA results, optical-tensor calculation records, and independent HSE-NEP validation data.

CODE AVAILABILITY

The Python analysis scripts are publicly available in the accompanying code archive at https://doi.org/10.24435/materialscloud:yh-wt. They include scripts for extracting trajectory observables, evaluating Green–Kubo electro-optic response functions, plotting spectra, and performing complex Debye fits.

ACKNOWLEDGMENTS

This work was supported by the National Key Research and Development Program of China (Grant No. 2024YFA1408200), the National Natural Science Foundation of China (Grant Nos. T2293700 and T2293702), and the Strategic Priority Research Program of the Chinese Academy of Sciences (Grant No. XDB1440101).

AUTHOR CONTRIBUTIONS

M.W. wrote the manuscript, developed the code, performed the calculations, and analyzed the data. L.-W.W. provided scientific guidance and contributed to revising the manuscript.

COMPETING INTERESTS

The authors declare no competing interests.

REFERENCES

[1] M. Zgonik, P. Bernasconi, M. Duelli, R. Schlesser, P. G"unter, M. H. Garrett, D. Rytz, Y. Zhu, and X. Wu, Dielectric, elastic, piezoelectric, electro-optic, and elasto-optic tensors of BaTiO3 crystals, Physical Review B **50**, 5941 (1994).

[2] S. Abel, F. Eltes, J. E. Ortmann, A. Messner, P. Castera, T. Wagner, D. Urbonas, A. Rosa, A. M. Gutierrez, D. Tulli, P. Ma, B. Baeuerle, A. Josten, W. Heni, D. Caimi, L. Czornomaz, A. A. Demkov, J. Leuthold, P. Sanchis, and J. Fompeyrine, Large pockels effect in micro- and nanostructured barium titanate integrated on silicon, Nature Materials **18**, 42 (2019).

[3] D. Chelladurai, M. Kohli, J. Winiger, D. Moor, A. Messner, Y. Fedoryshyn, M. Eleraky, Y. Liu, H. Wang, and J. Leuthold, Barium titanate and lithium niobate permittivity and pockels coefficients from megahertz to sub-terahertz frequencies, Nature Materials **24**, 868 (2025).

[4] P. Ghosez, X. Gonze, and J.-P. Michenaud, Ab initio phonon dispersion curves and interatomic force constants of barium titanate, Ferroelectrics **206**, 205 (1998).

[5] M. Veithen, X. Gonze, and P. Ghosez, First-principles study of the electro-optic effect in ferroelectric oxides, Physical Review Letters **93**, 187401 (2004).

[6] M. Veithen, X. Gonze, and P. Ghosez, Nonlinear optical susceptibilities, raman efficiencies, and electro-optic tensors from first-principles density functional perturbation theory, Physical Review B **71**, 125107 (2005).

[7] A. K. Hamze and A. A. Demkov, First-principles study of the linear electro-optical response in strained SrTiO3, Physical Review Materials **2**, 115202 (2018).

[8] I. Kim, T. Paoletta, and A. A. Demkov, Nature of electro-optic response in tetragonal BaTiO3, Physical Review B **108**, 115201 (2023).

[9] G. Shirane, J. D. Axe, J. Harada, and A. Linz, Inelastic neutron scattering from single-domain BaTiO3, Physical Review B **2**, 3651 (1970).

[10] M. Kotiuga, S. Halilov, B. Kozinsky, M. Fornari, N. Marzari, and G. Pizzi, Microscopic picture of paraelectric perovskites from structural prototypes, Physical Review Research **4**, L012042 (2022).

[11] V. de Mestral, L. Bastonero, M. Kotiuga, M. Mladenović, N. Marzari, and M. Luisier, Ab initio functional-independent calculations of the clamped pockels tensor of tetragonal barium titanate, Physical Review B **111**, 184306 (2025).

[12] L. Walizer, S. Lisenkov, and L. Bellaiche, Finite-temperature properties of (Ba,Sr)TiO_3 systems from atomistic simulations, Physical Review B **73**, 144105 (2006).

[13] I. Ponomareva, L. Bellaiche, T. Ostapchuk, J. Hlinka, and J. Petzelt, Terahertz dielectric response of cubic $BaTiO_3$, Physical Review B **77**, 012102 (2008).

[14] J. Hlinka, T. Ostapchuk, D. Nuzhnyy, J. Petzelt, P. Kužel, C. Kadlec, P. Vaněk, I. Ponomareva, and L. Bellaiche, Coexistence of the phonon and relaxation soft modes in the terahertz dielectric response of tetragonal $BaTiO_3$, Physical Review Letters **101**, 167402 (2008).

[15] A. Ross, M. S. M. M. Ali, A. Saha, R. Zu, V. Gopalan, I. Dabo, and L.-Q. Chen, Thermodynamic theory of linear optical and electro-optical properties of ferroelectrics, Physical Review B **111**, 085109 (2025).

[16] A. Ross, A. Frazer, V. Gopalan, and L.-Q. Chen, A dynamical phase-field model for the optical properties of ferroelectrics, arXiv preprint arXiv:2607.16180 10.48550/arXiv.2607.16180

(2026), arXiv:2607.16180 [cond-mat.mtrl-sci].

[17] Y. Liu, G. Ren, T. Cao, R. Mishra, and J. Ravichandran, Modeling temperature, frequency, and strain effects on the linear electro-optic coefficients of ferroelectric oxides, Journal of Applied Physics **131**, 163101 (2022).

[18] L. Gigli, M. Veit, M. Kotiuga, G. Pizzi, N. Marzari, and M. Ceriotti, Thermodynamics and dielectric response of batio3 by data-driven modeling, npj Computational Materials **8**, 209 (2022).

[19] E. Stocco, C. Carbogno, and M. Rossi, Electric-field driven nuclear dynamics of liquids and solids from a multi-valued machine-learned dipolar model, npj Computational Materials **11**, 304 (2025).

[20] R. Kubo, Statistical-mechanical theory of irreversible processes. i. general theory and simple applications to magnetic and conduction problems, Journal of the Physical Society of Japan **12**, 570 (1957).

[21] L. Monacelli, R. Bianco, M. Cherubini, M. Calandra, I. Errea, and F. Mauri, The stochastic self-consistent harmonic approximation: calculating vibrational properties of materials with full quantum and anharmonic effects, Journal of Physics: Condensed Matter **33**, 363001 (2021).

[22] R. Masuki, T. Nomoto, R. Arita, and T. Tadano, Ab initio structural optimization at finite temperatures based on anharmonic phonon theory: Application to the structural phase transitions of batio3, Physical Review B **106**, 224104 (2022).

[23] L. Monacelli and N. Marzari, Electrostatic interactions in atomistic and machine-learned potentials for polar materials, Physical Review B **113**, 094101 (2026).

[24] N. Goldenfeld, *Lectures on Phase Transitions and the Renormalization Group* (Addison-Wesley, Reading, MA, 1992).

[25] F. Cordero, F. Craciun, P. S. da Silva, Jr., M. Venet Zambrano, E. Mercadelli, and P. Galizia, Oxygen vacancies in semiconducting $BaTiO_3$-based ferroelectrics: Electron doping, history dependence of T_C, and domain wall pinning, Physical Review B **111**, 054112 (2025).

[26] J. P. Perdew, K. Burke, and M. Ernzerhof, Generalized gradient approximation made simple, Physical Review Letters **77**, 3865 (1996).

[27] J. Heyd, G. E. Scuseria, and M. Ernzerhof, Hybrid functionals based on a screened coulomb potential, The Journal of Chemical Physics **118**, 8207 (2003).

[28] P. Giannozzi, S. Baroni, N. Bonini, M. Calandra, R. Car, C. Cavazzoni, D. Ceresoli, G. L. Chiarotti, M. Cococcioni, I. Dabo, A. Dal Corso, S. de Gironcoli, S. Fabris, G. Fratesi, R. Gebauer, U. Gerstmann, C. Gougoussis, A. Kokalj, M. Lazzeri, L. Martin-Samos, N. Marzari, F. Mauri, R. Mazzarello, S. Paolini, A. Pasquarello, L. Paulatto, C. Sbraccia, S. Scandolo, A. Smogunov, P. Umari, and R. M. Wentzcovitch, Quantum espresso: a modular and open-source software project for quantum simulations of materials, Journal of Physics: Condensed Matter **21**, 395502 (2009).

[29] P. Giannozzi, O. Andreussi, T. Brumme, O. Bunau, M. Calandra, R. Car, C. Cavazzoni, D. Ceresoli, M. Cococcioni, I. Dabo, A. Dal Corso, S. de Gironcoli, P. Delugas, A. Di Stasio, A. Ferretti, A. Floris, G. Fratesi, G. Fugallo, R. Gebauer, U. Gerstmann, A. Giannozzi, Y. Gillet, J. D. Gouveia, M. Gusso, A. Kokalj, M. Lazzeri, M. Marsili, L. Martin-Samos, N. Marzari, F. Mauri, H.-V. Nguyen, A. O. Nguyen, L. Paulatto, S. Poncé, D. Rocca, R. Sabatini, B. Santra, M. Schlipf, A. P. Seitsonen, A. Smogunov, I. Timrov, P. Umari, and R. M. Wentzcovitch, Advanced capabilities for materials modelling with quantum espresso, Journal of Physics: Condensed Matter **29**, 465901 (2017).

[30] S. P. Huber, S. Zoupanos, M. Uhrin, L. Talirz, L. Kahle, *et al.*, Aiida 1.0, a scalable computational infrastructure for automated reproducible workflows and data provenance, Scientific Data **7**, 300 (2020).

[31] M. Uhrin, S. P. Huber, J. Yu, N. Marzari, and G. Pizzi, Workflows in aiida: Engineering a high-throughput, event-based engine for robust and modular computational workflows, Computational Materials Science **187**, 110086 (2021).

[32] L. Bastonero and N. Marzari, Automated all-functionals infrared and raman spectra, npj Computational Materials **10**, 55 (2024).

[33] R. Resta, Macroscopic polarization in crystalline dielectrics: the geometric phase approach, Reviews of Modern Physics **66**, 899 (1994).

[34] I. Souza, J. Íniguez, and D. Vanderbilt, First-principles approach to insulators in finite electric fields, Physical Review Letters **89**, 117602 (2002).

[35] P. Umari and A. Pasquarello, Ab initio molecular dynamics in a finite homogeneous electric field, Physical Review Letters **89**, 157602 (2002).

[36] D. R. Hamann, M. Schlüter, and C. Chiang, Norm-conserving pseudopotentials, Physical Review Letters **43**, 1494 (1979).

[37] D. R. Hamann, Optimized norm-conserving vanderbilt pseudopotentials, Physical Review B **88**, 085117 (2013).

[38] M. Schlipf and F. Gygi, Optimization algorithm for the generation of oncv pseudopotentials, Computer Physics Communications **196**, 36 (2015).

[39] W. Jia, Z. Cao, L. Wang, X. Chi, W. Gao, and L.-W. Wang, The analysis of a plane wave pseudopotential density functional theory code on a gpu machine, Computer Physics Communications **184**, 9 (2013).

[40] W. Jia, J. Fu, Z. Cao, L. Wang, X. Chi, W. Gao, and L.-W. Wang, Fast plane wave density functional theory molecular dynamics calculations on multi-gpu machines, Journal of Computational Physics **251**, 102 (2013).

[41] J. Qi, T. W. Ko, B. C. Wood, T. A. Pham, and S. P. Ong, Robust training of machine learning interatomic potentials with dimensionality reduction and stratified sampling, npj Computational Materials **10**, 43 (2024).

[42] W. Zhang, X. Wu, C. Wang, S. Hu, Y. Liu, and L.-W. Wang, Constructing machine learning interatomic potentials with minimum amount of ab initio data, npj Computational Materials **12**, 174 (2026).

[43] I. Batatia, D. P. Kovács, G. N. C. Simm, C. Ortner, and G. Csányi, Mace: Higher order equivariant message passing neural networks for fast and accurate force fields, in *Advances in Neural Information Processing Systems*, Vol. 35 (2022) pp. 11423–11436.

[44] N. Gönnheimer, K. Reuter, V. Kapil, and J. T. Margraf, Mace-mdp: A general dipole and polarizability model for organic molecules and materials (2025).

[45] Z. Fan, Z. Zeng, C. Zhang, Y. Wang, K. Song, H. Dong, Y. Chen, and T. Ala-Nissila, Neuroevolution machine learning potentials: Combining high accuracy and low cost in atomistic simulations and application to heat transport, Physical Review B **104**, 104309 (2021).

[46] Z. Fan, W. Zhang, Z. Zhang, K. Xu, X. Shao, and H. Dong, Nep-cg and nep-aacg: Efficient coarse-grained and multiscale all-atom-coarse-grained neuroevolution potentials, Computational Materials Today **10**, 100055 (2026).

Supplementary Files

This is a list of supplementary files associated with this preprint. Click to download.

- support.pdf